8-22-2009

PAH Emission from Ultraluminous Infrared Galaxies

V. Desai
California Institute of Technology

L. Armus
Spitzer Science Center

H. W. W. Spoon
Cornell University

V. Charmandaris
University of Crete

J. Bernard-Salas
Cornell University

See next page for additional authors

Accepted for publication in ApJ
Preprint typeset using LaTeX style emulateapj v. 08/22/09

PAH EMISSION FROM ULTRALUMINOUS INFRARED GALAXIES[1]

V. Desai[2], L. Armus[3], H.W.W. Spoon[4], V. Charmandaris[5,6], J. Bernard-Salas[4], B.R. Brandl[7], D. Farrah[4], B.T. Soifer[2,3], H.I. Teplitz[3], P.M. Ogle[3], D. Devost[4], S.J.U. Higdon[8], J.A. Marshall[4], J.R. Houck[4]

Accepted for publication in ApJ

ABSTRACT

We explore the relationships between the Polycyclic Aromatic Hydrocarbon (PAH) feature strengths, mid-infrared continuum luminosities, far-infrared spectral slopes, optical spectroscopic classifications, and silicate optical depths within a sample of 107 ULIRGs observed with the Infrared Spectrograph on the *Spitzer Space Telescope*. The detected 6.2 μm PAH equivalent widths (EQWs) in the sample span more than two orders of magnitude ($\sim$0.006–0.8 μm), and ULIRGs with HII-like optical spectra or steep far-infrared spectral slopes ($S_{25}/S_{60} < 0.2$) typically have 6.2 μm PAH EQWs that are half that of lower-luminosity starbursts. A significant fraction ($\sim$40–60%) of HII-like, LINER-like, and cold ULIRGs have very weak PAH EQWs. Many of these ULIRGs also have large ($\tau_{9.7} > 2.3$) silicate optical depths. The far-infrared spectral slope is strongly correlated with PAH EQW, but not with silicate optical depth. In addition, the PAH EQW decreases with increasing rest-frame 24 μm luminosity. We argue that this trend results primarily from dilution of the PAH EQW by continuum emission from dust heated by a compact central source, probably an AGN. High luminosity, high-redshift sources studied with *Spitzer* appear to have a much larger range in PAH EQW than seen in local ULIRGs, which is consistent with extremely luminous starburst systems being absent at low redshift, but present at early epochs.

Subject headings: infrared:galaxies – galaxies:active – galaxies:starburst

1. INTRODUCTION

Ultraluminous Infrared Galaxies (ULIRGs) have bolometric luminosities comparable to quasars ($L_{bol} \gtrsim 10^{12}$ $L_\odot$), but emit nearly all of this energy at mid- and far-infrared wavelengths. Although ULIRGs are rare in the local Universe and comprise only a few percent of infrared-bright galaxies (Soifer et al. 1987; Sanders et al. 2003), they account for a rapidly increasing fraction of all star-formation activity at high-redshift, and they may dominate the far-infrared background at $z > 2$ (Franceschini et al. 2001; Le Floc'h et al. 2005; Pérez-González et al. 2005). It has been suggested that they play a role in the formation of both quasars and elliptical galaxies (Kormendy & Sanders 1992; Sanders & Mirabel 1996; Scott et al. 2002).

To understand the roles that ULIRGs play in the formation of massive galaxies, the global star formation history of the universe, and the creation of the cosmic infrared background, it is essential to determine the extent to which Active Galactic Nuclei (AGN) and star formation contribute to their enormous luminosities. Several studies have used optical (de Grijp et al. 1985; Osterbrock & De Robertis 1985; Armus et al. 1987, 1989; Veilleux et al. 1995; Kim et al. 1998; Veilleux et al. 1999a) and near-infrared (Goldader et al. 1995; Veilleux et al. 1997, 1999b; Murphy et al. 1999, 2001; Burston et al. 2001; Davies et al. 2003; Dannerbauer et al. 2005) spectroscopy to determine the main source of ionization of the line-emitting gas in local ULIRGs. These studies show that while the majority of ULIRGs have optical and near-infrared spectra similar to those of starburst galaxies, the fraction of ULIRGs displaying the spectroscopic signatures of an AGN, either broad permitted lines or high-ionization narrow-lines, increases with infrared luminosity. In addition, evidence for AGN activity is more commonly found among ULIRGs with flatter far-infrared spectral slopes (those classified as "warm" with $S_{25}/S_{60} \geq 0.2$ as measured with IRAS), than among ULIRGs with steeper far-infrared spectral slopes (those classified as "cold" with $S_{25}/S_{60} < 0.2$).

A principle uncertainty of these optical and near-infrared studies is the extent to which the physical conditions of the visible gas are linked to those in the deeply embedded nucleus, where the bulk of the energy is generated (Soifer et al. 2000). Emission at longer wavelengths can penetrate more heavily obscured regions close to the nuclear power source. Therefore, diagnostics derived from mid-infrared spectroscopy are potentially a better probe of the dominant energy source in the nuclear regions. The mid-infrared spectra of ULIRGs are comprised of continuum emission from heated dust grains; broad emission features associated with Polycyclic Aromatic Hydrocarbons (PAHs), the most prominent of which appear at 6.2, 7.7, 8.6, 11.3, and 12.7 μm; ab-

[1] Based on observations obtained with the *Spitzer Space Telescope*, which is operated by the Jet Propulsion Laboratory, California Institute of Technology, under NASA contract 1407
[2] Division of Physics, Math & Astronomy, California Institute of Technology, Pasadena, CA 91125
[3] Spitzer Science Center, MS 220-6, Caltech, Pasadena, CA 91125
[4] Cornell University, Ithaca, NY 14853
[5] University of Crete, Department of Physics, P.O. Box 2208 GR-71003, Heraklion, Greece
[6] IESL/Foundation for Research and Technology - Hellas, GR-71110, Heraklion, Greece and Chercheur Associé, Observatoire de Paris, F-75014, Paris, France
[7] Leiden University, P.O. Box 9513, 2300 RA Leiden, The Netherlands
[8] Georgia Southern University, Statesboro, GA 30460
[9] The IRS was a collaborative venture between Cornell University and Ball Aerospace Corporation funded by NASA through the Jet Propulsion Laboratory and the Ames Research Center

sorption by amorphous silicates centered at 9.7 and 18 μm; and atomic fine-structure lines of Ne, O, Si, and S covering a large range in ionization potential. Diagnostic diagrams using combinations of fine-structure line ratios, mid-infrared spectral slope, and PAH feature strengths have been used to classify bright ULIRGs, based on the expectations that ULIRGs with central AGN produce high ionization lines, have flatter spectral slopes, and display lower PAH equivalent widths than those without (e.g. Genzel et al. 1998; Lutz et al. 1998; Rigopoulou et al. 1999; Laurent et al. 2000; Tran et al. 2001; Sturm et al. 2002; Armus et al. 2004, 2006, 2007; Farrah et al. 2007). For sources at high-redshift ($z \geq 1$), however, it is generally not possible to place useful limits on the high-ionization fine-structure lines. The PAH emission, together with the infrared spectral slope, are often the only mid-infrared diagnostics available for studying high-redshift ULIRGs.

The first attempts to classify the energy generation mechanism in ULIRGs using mid-infrared PAH features made use of data from the *Infrared Space Observatory* (Lutz et al. 1998, 1999; Rigopoulou et al. 1999; Tran et al. 2001). For these studies, ULIRGs were classified based on the strengths of their 7.7 μm PAH line-to-continuum ratios (L/C, defined as the ratio of the peak height of the 7.7 μm PAH feature to the level of the underlying 7.7 μm continuum). The PAH-based classifications showed that most ($\sim$80%) ULIRGs have strong PAH emission indicative of star formation as the dominant power source. However, the highest luminosity sources tend to have weak (or undetected) PAH emission, interpreted as a sign of increased AGN activity. Recently, Imanishi et al. (2007) analyzed the mid-infrared spectra of 48 nearby ULIRGs observed with the Infrared Spectrograph (IRS; Houck et al. 2004) on board the *Spitzer Space Telescope*. These authors suggest that 30-50% of these ULIRGs, all of which have HII-like or LINER-like optical classifications, harbor buried AGN.

In this paper we present the mid-infrared spectroscopic properties of a large sample of 107 ULIRGs that comprise the IRS GTO team ULIRG survey. The sample includes a large fraction ($\sim$40%) of warm sources, which tend to have higher infrared luminosities than cold ULIRGs. The warm ULIRGs are a critical population to study, since it has been suggested that they mark the transition between staburst-dominated ULIRGs and QSOs (e.g. Sanders et al. 1988b). Because of their high luminosities, they provide a much-needed baseline over which to extrapolate to the extremely high luminosities ($L_{IR} > 10^{13}$ $L_{\odot}$) seen at higher redshift.

The sensitivity of the IRS offers two distinct advantages over previous studies with ISO. First, we can measure the PAH strengths with respect to the dust continuum (the equivalent width, or hereafter EQW) over nearly two orders of magnitude, allowing us to quantify the PAH emission in many ULIRGs that previously only had upper limits. This is critical for fitting trends with luminosity and spectral slope, as many ULIRGs have much weaker PAH emission features than are typically found in low-luminosity starburst galaxies (see §3.1). Second, the Short-Low and Long-Low IRS modules (5–38 μm) offer greatly increased wavelength coverage compared to ISOPHOT-S, allowing us to accurately fit the silicate absorption (at 9.7 and 18 μm) and multiple PAH features in all the ULIRGs. Here, we have chosen to fit the 9.7 μm silicate absorption feature since it is the strongest and the 6.2 and 11.3 μm PAH features because they are both well-isolated and easily measured. Previously the 7.7 μm feature was often used, which is not ideal because absorption at both shorter and longer wavelengths can mimic a peak at 7.7 μm (Spoon et al. 2002) and its integrated flux can be difficult to measure due to blending with the adjacent 8.6 μm feature. By correlating the PAH emission with the silicate absorption, it is possible to gain insight into the distribution of the heating source(s) and the grains. In the following analysis, we use $H_0 = 70$ km s^{-1} Mpc^{-1}, $\Omega_m = 0.3$, and $\Lambda = 0.70$.

2. OBSERVATIONS & DATA REDUCTION

The 107 ULIRGs presented in this paper were chosen primarily from the IRAS 1-Jy survey (Kim et al. 1998), the IRAS 2-Jy survey (Strauss et al. 1992), and the FIRST/IRAS radio-far-infrared sample of Stanford et al. (2000). The ULIRGs span a redshift range of $0.018 < z < 0.93$, have IRAS 60 μm flux densities between $0.14 < S_{60}/\mathrm{Jy} < 103$, and have integrated 40–500 μm luminosities in the range $11.7 < \log(L_{FIR}/L_{\odot}) < 13.13$. The sample consists of 41 warm ULIRGs and 66 cold ULIRGs, based upon their rest-frame far-infrared flux densities at 25 and 60 μm. Many of our highest luminosity sources were taken from the Stanford et al. (2000) FIRST/IRAS survey. While radio-bright AGN may preferentially populate the highest luminosities of the Stanford et al. survey, the selected ULIRGs have radio to far-infrared flux density ratios consistent with infrared-selected starburst galaxies of lower luminosity. The sample is specifically designed to include a larger fraction of warm and infrared luminous sources than would be found in a pure flux- or volume-limited sample, for the express purpose of allowing a careful study of the mid-infrared spectral properties as functions of infrared color and luminosity.

All ULIRGs were observed in Staring Mode with both sub-slits (orders) of each of the Short-Low (SL) and Long-Low (LL) modules of the IRS. Each target was acquired by performing a high accuracy IRS peak-up on the target itself, or by peaking up on a nearby 2MASS star and offsetting to the target. Each galaxy was observed at two nod positions within each of the IRS sub-slits (SL1, SL2, LL1, LL2). The resulting spectra have a spectral resolution of R $\sim$ 80 over the 5–38 μm wavelength range.

All spectra were reduced using the S14 IRS pipeline at the Spitzer Science Center. This reduction includes ramp fitting, dark sky subtraction, droop correction, linearity correction, and wavelength and flux calibration. The flux calibration sources were HD173511 for the SL and LL2 modules and KsiDra for the LL1 module. For a given module, order, and nod position, the background in the two-dimensional spectrum was removed by subtracting the combined two-dimensional data taken with the same module, but adjacent order. One-dimensional spectra were extracted from the background-subtracted two-dimensional spectra using the SMART data reduction package (Higdon et al. 2004). The adopted extraction apertures are four pixels at the blue end of each order and expand linearly with wavelength.

The 6.2 and 11.3 μm PAH features were measured by

integrating the flux above a spline-interpolated continuum. For those sources with strong 6 μm water ice absorption, the apparent 6.2 μm EQW has been corrected by using an inferred 6.2 μm continuum defined by a spline interpolation between 5–26 μm, using pivot points at 5.2, 5.6, 7.8 (in the case of very weak PAH emission), 14, and 26 μm. This correction results in a lower 6.2 μm PAH EQW, and is correct under the assumption that the PAH emission is unaffected by the bulk of the ice absorption. A full description of the ice-fitting procedure is given by Spoon et al. (2007), who first present the measured 6.2 μm EQWs for many of these ULIRGs (see §3.2 and Figure 2 for a description of the correction and Figure 1 for an indication of the size of the correction). The PAH emission at 11.3 μm is affected by the broad 9.7 μm silicate absorption feature, which can be deep in ULIRGs. However, lacking a strong understanding of how the obscuring dust is distributed, we have not attempted to correct for it. Of the 107 ULIRGs analyzed in this paper, the 6.2 μm PAH feature is detected for all but 11 sources, and the 11.3 μm PAH feature is detected for all but 12 sources.

In the following, we investigate the variation of the PAH features with rest-frame continuum fluxes at 5.5, 24, 25, and 60 μm. The 5.5 μm flux is taken to be the average continuum betweeen 5.3 and 5.8 μm. The 24 μm flux was calculated by convolving the IRS spectrum with the MIPS 24 μm bandpass. In the 10 cases where the IRS spectrum did not extend over the full wavelength range of the wide IRS bandpass due to trimming of pipeline artifacts (e.g. fringes), it was extended by linearly interpolating in log-log space between the IRS spectrum and the 60 μm IRAS flux density (Moshir 1990). No color-correction was made to place these filter fluxes on the MIPS absolute scale, but these corrections are small (<5%) based on the spectral shape of the ULIRGs within the 24 μm bandpass (see the MIPS Data Handbook). The 25 μm rest-frame flux was estimated by taking the median of the trimmed and (when needed) interpolated IRS spectrum between 24.7 and 25.3 μm. The rest-frame 60 μm luminosity was estimated by linearly interpolating in log-log space between the observed IRAS 60 and 100 μm flux densities. For 12 ULIRGs, this interpolation likely underestimates the 60 μm luminosity, either because the object is at a redshift high enough ($z > 0.65$) that the observed 100 μm IRAS observation corresponds to a rest-frame wavelength less than 60 μm, or because the 100 μm observation resulted in only a limit, rather than a detection.

Classifications based on optical spectra are available from the literature for 64 of the 107 ULIRGs in our sample. Of these, 15 have HII-like optical spectra, 22 are LINER-like, and 27 are Seyfert-like.

3. RESULTS

3.1. *PAH strength and silicate absorption versus spectral slope and optical classification*

The median IRS spectra for warm and cold ULIRGs are shown in the left-hand panel of Figure 1. Cold ULIRGs have a median 6.2 μm PAH EQW that is a factor of six higher than the median measured for warm ULIRGs (0.24 versus 0.04 μm; see Table 1). The right-hand panel of Figure 1 shows the average starburst spectrum from Brandl et al. (2006) plotted over the median cold ULIRG spectrum. Cold ULIRGs have a median 6.2 μm PAH EQW which is about half the median for lower-luminosity starbursts (see also Imanishi et al. (2007)). The difference in the PAH EQWs in the median warm and cold ULIRG spectra reflects the strong trend between PAH EQW and mid-infrared spectral type shown in Figure 2. There is a huge range in measured PAH EQW among the sample ULIRGs. The full range in PAH EQW for those ULIRGs with detected emission is 0.006–0.864 μm for the 6.2 μm feature, and 0.006–1.169 μm for the 11.3 μm feature. The smallest upper limits are 0.005 and 0.004 μm for the 6.2 and 11.3 μm features, respectively. While the median 6.2 μm PAH EQW among cold/HII ULIRGs is about half as large as for local starburst galaxies, the median 11.3 μm PAH EQW in cold/HII ULIRGs is 80% of that measured in starburst galaxies. The cold ULIRGs and starburst galaxies track each other over the limited range of $0.06 < S_{25}/S_{60} < 0.2$ (see Figure 2).

Figure 1 also demonstrates that the median cold source shows stronger silicate absorption at both 9.7 and 18 μm than the median warm source (1.36 versus 0.65 for $\tau_{9.7}$, the optical depth at 9.7 μm), and the median cold ULIRG has stronger absorption than the average starburst (1.36 versus 0.22). In Figure 3, we plot the apparent silicate optical depth as a function of far-infrared spectral slope. While the ULIRGs with $\tau_{9.7} > 1$ have steeper far-infrared spectra than the sources with $\tau_{9.7} < 1$, we find no real correlation (see also Imanishi et al. (2007); Hao et al. (2007)). In fact, many sources with very high silicate optical depths ($\tau_{9.7} > 2$) would also be classified as warm ULIRGs. All of the ULIRGs with Seyfert-1 optical spectra, and many, but not all, of the ULIRGs with Seyfert-2 optical spectra have $\tau_{9.7} < 1$ and $S_{25}/S_{60} > 0.2$.

The median HII, LINER, and Seyfert ULIRG IRS spectra are shown in the left-hand panel of Figure 4. The median and mean values of the 6.2 and 11.3 μm PAH EQW for each of these spectral classes is given in Table 1. As expected, the HII-like ULIRGs have the largest median 6.2 μm PAH EQW (0.28 μm) while the ULIRGs classified as Seyferts have the lowest (0.04 μm). The median PAH EQW for infrared cold ULIRGs is comparable to the median for those classified as HII-like, while the median PAH EQW for infrared warm sources is similar to the median for Seyfert-like ULIRGs. There are a number of ULIRGs with HII-like or LINER-like spectra that have unusually low 6.2 μm PAH EQW ($\lesssim$0.15 μm, or about 1/4 that found for pure starburst galaxies). Of the 22 LINER-like (15 HII-like) ULIRGs in the sample, 12 (six) have 6.2 μm PAH EQW $\leq$ 0.15 μm. Similarly, of the 66 cold ULIRGs, 23 have a 6.2 μm PAH EQW $\leq$ 0.15 μm.

The right-hand panel of Figure 4 shows the median HII and LINER ULIRG spectra overplotted with the average starburst spectrum from Brandl et al. (2006) and the average infrared-bright LINER spectrum from Sturm et al. (2006). Although sources with HII-like optical spectra have the largest PAH EQWs among ULIRGs, the median values are only about 50% of those measured for pure starburst galaxies, the same result as found for the cold ULIRGs. HII-like ULIRGs also have stronger silicate absorption at 9.7 and 18 μm than seen in lower-

luminosity starbursts (1.52 versus 0.22 for $\tau_{9.7}$). Compared to infrared-bright LINERs, LINER-like ULIRGs have $\sim$ 25% smaller PAH EQWs, and stronger silicate absorption ($\tau_{9.7} = 2.11$ for the LINER-like ULIRGs while it is only 0.84 for the IR-bright LINERs).

3.2. *PAH equivalent width versus continuum luminosity*

In Figure 5, we plot the 6.2 and 11.3 μm PAH EQW versus 24 μm rest-frame luminosity. This continuum wavelength was chosen because it samples the peak emission of warm ($\sim$120 K) thermally-emitting dust, it can be measured much more accurately than LIR in many cases, it is free from strong emission or absorption features, and it allows direct comparison to a variety of low-redshift samples observed with the MIPS 24 μm filter and to $z \sim 2$ samples observed with the MIPS 70 μm filter. For reference, we estimate that $\log_{10}(\nu L_\nu(24\mu\mathrm{m})/\mathrm{LIR}) = -1.06 \pm 0.47$ for cold ULIRGs and -0.79 ± 0.38 for warm ULIRGs. These estimates were made by applying the Sanders & Mirabel (1996) prescription for converting IRAS photometry into LIR to the nearest ($z < 0.2$) ULIRGs in our sample. Figure 5 shows a trend of decreasing 6.2 and 11.3 μm PAH EQW with increasing rest-frame 24 μm luminosity. There is significant scatter in this relation, and ULIRGs with low PAH EQW span a wide range in luminosity. Nevertheless, the presence of a correlation is verified by a highly significant Spearman correlation coefficient, whether or not upper limits are included in the same way as detections in the calculation.

We have divided the ULIRG sample into six luminosity bins chosen to span the full range in 24 μm luminosity ($(0.03 - 8) \times 10^{12}$ L$_\odot$), and to contain approximately equal numbers (17-18) of ULIRGs. The median 6.2 and 11.3 μm PAH EQWs drop by an order of magnitude between the first and last luminosity bins (see Table 2). The median ULIRG spectrum in each 24 μm luminosity class is shown in Figure 6. The median spectra were constructed using all sources in a given luminosity bin, even those for which only an upper limit on the PAH EQW could be measured. Moving from lowest to highest 24 μm luminosity (top to bottom in Figure 6), the PAH features diminish and the spectrum flattens. While the median spectrum in the highest luminosity bin has a noticeably smaller silicate absorption than the lower-luminosity median spectra, there is a large range in the apparent silicate optical depth among the most luminous sources. This is consistent with the results of Spoon et al. (2007), who find a dichotomy in silicate optical depths among sources with small 6.2 μm PAH EQW (see also §3.3).

3.3. *Silicate absorption versus PAH equivalent width*

Figure 7 shows the silicate optical depth versus 6.2 μm PAH EQW for the ULIRGs in our sample. Such a plot was first presented by Spoon et al. (2007), who discussed the presence of two discrete tracks, or branches. Figure 7 shows that the horizontal branch is populated almost exclusively by infrared warm sources, while the diagonal branch is populated by about half of the warm sources and virtually all of the cold sources. Examining the ULIRGs for which we have optical spectroscopic classifications, the diagonal branch harbors about half of the Seyfert-like ULIRGs, and nearly all of the HII-like and LINER-like ULIRGs. The horizontal branch is populated mainly by ULIRGs showing Seyfert-like spectra, including all of the Type I sources. ULIRGs with Seyfert Type 2 optical spectra are found on both branches, spanning (nearly) the full range in silicate optical depth. Most of the ULIRGs without optical spectroscopic classifications lie on the diagonal branch. As noted in §3.1, a significant fraction of the HII and LINER-like ULIRGs have very low 6.2 μm PAH EQWs ($\leq$0.15 μm). Of these, almost all of the LINERs (11/12) and half (3/6) of the HII-like ULIRGs have $\tau_{9.7} \geq 2.5$, implying $A_V \geq 45$ mag.

4. DISCUSSION

The median 6.2 μm PAH EQWs of cold (or HII-like) ULIRGs is about 50% of that seen in lower-luminosity starbursts. Warm ULIRGs have 6.2 μm PAH EQWs that are up to two orders of magnitude smaller than those found in starbursts. There are several possible explanations for the extremely large range in PAH EQW and the overall low PAH EQW in ULIRGs compared to starbursts. Some ULIRGs may host a central AGN, and the associated soft X-ray and ultraviolet radiation may destroy PAH molecules (e.g. Aitken & Roche 1985; Voit 1992), or thermalize the emission. The AGN may also heat dust to significant temperatures (>400 K), resulting in excess continuum emission which would lower the measured 6.2 μm PAH EQW, in efffect diluting the starburst-driven PAH emission with respect to the AGN-powered, hot dust continuum. For either of these explanations, 55 ± 13% of the LINER-like ULIRGs and 40 ± 15% of the HII-like ULIRGs in our sample would harbor buried AGN. In comparison, Lutz et al. (1999) find the percentage of LINER-like ULIRGs classified by ISO as AGN to be 17 ± 15% and the percentage of HII-like ULIRGS classified by ISO as AGN to be 20 ± 12%. We are thus finding a much higher fraction of LINERs and HII-like ULIRGs with weak PAH emission, although, given the small sample sizes and the fact that the percentage is comparable to the statistical errors in the ISO sample, our results are formally consistent with those of Lutz et al. (1999) at the 2σ level. Our results are more comparable to those of Imanishi et al. (2007), who find that 30–50% of HII- and LINER-like ULIRGs contain dominant buried AGN. Of the 12 LINER-like and 6 HII-like ULIRGs with low PAH EQWs, 9 were observed with the high-resolution modules of the IRS (Farrah et al. 2007). Of these, none have detectable [NeV]14.3μm, [NeV]24.3μm, or [OIV]24.9μm line emission. Upper limits on the [NeV]14.3μm to [NeII]12.8μm line flux ratio range from 0.02 to 0.3, corresponding to starburst-dominated ULIRGs with less than 5$-$25% AGN contribution (Armus et al. 2007). However, it is important to note that many of these sources are deeply buried, as evidenced by their large silicate optical depths (see §3.3). As a result, the [NeV]14.3μm emission may be highly extinguished. In addition, it is plausible that a completely buried starburst exists in these sources, as in NGC 1377 (Roussel et al. 2006).

The 6.2 μm PAH EQW in ULIRGs could also be (intrinsically) smaller than that found in pure starburst galaxies if star formation in ULIRGs is accompanied by larger quantities of hot dust emission than is typically found in lower-luminosity starbursts. The dust would then have to "see" more of the stellar radiation and compete more effectively for UV photons, thus raising its

average temperature, something that is not unreasonable given the compact nature of the infrared emission in ULIRGs. However, if this were the case, then both the 6.2 and the 11.3 μm PAH EQW would be similarly depressed. However, among cold ULIRGs, the median 11.3 μm PAH EQW is 80% of that found in starbursts, while the median 6.2 μm PAH EQW is only 50%. A combination of dilution and extinction offers a more likely explanation. In this scenario, the 6.2 μm PAH EQW is diluted by hot dust continuum produced by a central ionizing source interior to the star-forming regions. The dilution of the 11.3 μm PAH EQW is less significant because of its proximity to the broad silicate absorption feature at 9.7 μm. The hot dust continuum responsible for diluting the 6.2 μm PAH EQW is heavily extincted at 11.3 μm, and therefore does not readily dilute the 11.3 μm PAH EQW. This is seen in Figure 7. The left-hand panels show that the 6.2 μm PAH EQWs of ULIRGs on the upper branch deviate strongly from the starbursts. In contrast, the right-hand panels indicate that ULIRGs have nearly starburst-like 11.3 μm PAH EQWs because the strong extinction at this wavelength overwhelms all but the strongest contribution from hot dust.

Finally, extinction is not likely to play a large role in the reduced 6.2 μm PAH EQWs found in ULIRGs compared to starbursts. Although ULIRGs on average display stronger silicate absorption features than lower-luminosity starbursts, larger column densities of dust would lead to depressed PAH EQWs only if the PAH emission were more extinguished than the continuum. Such a situation is unlikely, since the continuum flux is emitted by hot dust that must lie close to the ionization source.

In a further attempt to disentangle reduced PAH emission from increased hot dust emission as the driving force behind the low 6.2 μm PAH EQWs in ULIRGs, we plot the 6.2 μm PAH luminosity against the rest-frame 5.5 μm luminosity in Figure 8. Low-luminosity starbursts from Brandl et al. (2006) follow a correlation between these two quantities, characterized by $\log_{10}[\mathrm{L}(6.2\ \mu\mathrm{m\ PAH})] = -0.49 + 0.96 \times \log_{10}[\nu L_{\nu}(5.5\mu\mathrm{m})]$. ULIRGs do not lie on the extrapolation of this relation to higher luminosities. Instead, ULIRGs appear offset to higher 5.5 μm luminosities for their measured 6.2 μm PAH luminosities. Not surprisingly, sources with flatter far-infrared spectra and those with Seyfert-like optical spectra are, as a group, the most displaced towards higher 5.5 μm luminosity. However, the range of 6.2 μm PAH luminosity within the different classes (both optical and infrared) is the same. It has been suggested that an evolutionary link exists between ULIRGs and QSOs, such that cold ULIRGs evolve into warm ULIRGs on their way to becoming QSOs (e.g. Sanders et al. 1988a). Figure 8 implies that the transition between cold and warm ULIRGs involves primarily an increase in hot dust, rather than the suppression of PAH emission. Lutz et al. (1998) also suggested that dilution of the EQW by hot dust was the dominant effect among ULIRGs.

Also plotted in the lower left-hand panel of Figure 8 are $\sim$80 PG QSOs at $z < 0.5$ (Ogle & Antonucci 2007, in preparation; Shi et al. 2007, submitted). Most have only upper limits for the 6.2 micron PAH EQW, but 15 have detected values. The 5.5 μm continuum luminosities of ULIRGs and PG QSOs span the same range. The 15 PG QSOs with detected 6.2 μm PAH features show no evidence for a correlation in Figure 8. This is in contrast with the results of Schweitzer et al. (2006), who find a correlation between the 7.7 μm PAH luminosity and the 6 μm continuum luminosity among a sample of 25 PG QSOs, including 15 with upper limits on the PAH luminosity and 11 with detections. Based on the assumptions that the 6 μm luminosity is due to hot dust heated by an AGN, while the PAH luminosity is emitted by star-forming regions, they argue that their observed correlation is evidence for a starburst-AGN connection among PG QSOs. However, we find no such correlation when considering the 6.2 μm PAH feature.

While the flatter spectra and lower 6.2 μm PAH EQWs of many of the ULIRGs can readily be explained by an excess of hot dust emission, the silicate optical depth, at least in some cases, seems inconsistent with a simple model for the emission. The 9.7 μm silicate optical depth in ULIRGs varies from $-0.2 < \tau_{9.7} < 4$, and is on average deeper than in starburst galaxies. The radiative transfer models of Levenson et al. (2007) suggest that the geometry of the obscuring material in ULIRGs determines both the depth of the silicate feature and the infrared spectral slope. According to these models, the large apparent silicate optical depth ($\tau_{9.7} > 1$–2) observed in some ULIRGs requires an optically and geometrically thick, smooth dust component, since a clumpy dust distribution can only result in a shallow ($\tau_{9.7} < 1$) absorption feature. All of the Seyfert-like ULIRGs would then be viewed through this clumpy dust distribution, exhibiting flat infrared spectra, weak PAH EQWs, and shallow (or nonexistent) silicate absorption features. If this simple model is correct, a correlation between silicate optical depth and spectral slope might be expected. However, we find no such correlation (see Figure 3). In fact, a significant number of the sources with the most extreme absorption are warm (see Figure 7). These ULIRGs also tend to have low 6.2 μm PAH EQWs ($< 0.15\mu$m). A majority of the sources with large silicate optical depth are classified optically as LINERs.

Among local ULIRGs, the sources with the highest rest-frame 24 μm luminosities have the lowest 6.2 μm PAH EQWs (see Figure 5). The fit to this correlation is shown as the black line in Figure 9, and is given by $\log_{10}(6.2\ \mu\mathrm{m\ PAH\ EQW}[\mu\mathrm{m}]) = (7.71 \pm 0.07) + (-0.723 \pm 0.006) \times \log_{10}(\nu L_{\nu}(24\mu\mathrm{m})[L_{\odot}])$. According to this fit, ULIRGs with rest-frame 24 μm luminosities above about 10^{12} $L_{\odot}$ have 6.2 μm PAH EQWs below 0.1–0.2 μm. However, very luminous infrared sources with strong PAH emission (6.2 μm PAH EQW $>$ 0.3-0.5 μm) have recently been found in high-redshift samples that were selected in the submillimeter, which is dominated by cool dust emission (Lutz et al. 2005; Menéndez-Delmestre et al. 2007; Valiante et al. 2007). For example, of the five IRS spectra of submillimeter sources presented by Menéndez-Delmestre et al. (2007), two have the wavelength coverage to measure the 6.2 μm PAH feature. These two submillimeter-selected ULIRGs have rest-frame EQWs of approximately 0.6 and 0.8 μm, comparable to the strongest PAH emission measured for local starburst galaxies. Their positions are marked in Figure 9, and they are clearly well above the fit to the local ULIRGs. Additional examples have been found in samples selected at 160 μm (MIPSJ142824;

Desai et al. 2006) or a combination of 24 μm flux and mid-infrared color (Yan et al. 2005; Sajina et al. 2007). These are also plotted in Figure 9. However, sources with high rest-frame 24 μm luminosities and large 6.2 μm PAH EQW are rare in bright ($f_{24} > 0.7$ mJy) flux-limited samples selected at 24 μm (e.g. Houck et al. 2005; Weedman et al. 2006); these samples appear dominated by AGN. ULIRGs with high rest-frame 24 μm luminosities and strong PAH emission are absent from local samples, yet they obviously exist at high redshift, and they can be found by selecting on color, cold dust emission, or by probing to fainter flux levels in the mid-infrared (observed $f_{24} < 0.3$ mJy). At $z < 1$, the generation of large amounts of warm dust seems to require the presence of a dominant AGN. The absence of extremely luminous starburst-dominated ULIRGs at low redshift represents a real effect, and not simply an observational bias.

5. SUMMARY AND CONCLUSIONS

Using a large sample of 107 ULIRGs observed with the IRS on board the *Spitzer Space Telescope*, we investigate the relationships between the 6.2 and 11.3 μm PAH EQWs, continuum luminosity, infrared spectral slope, optical spectroscopic classification, and silicate optical depth. Our results can be summarized as follows:

1. There is an extremely large range in detected 6.2 μm PAH EQWs among ULIRGs, spanning more than two orders of magnitude from $\sim$0.006–0.9 μm. ULIRGs classified as starburst-dominated based on their far-infrared colors or optical spectra have median 6.2 μm PAH EQWs which are 50% of that measured in low-luminosity starburst galaxies. An excess of hot dust, which is most prominent in the far-infrared warm or Seyfert-like ULIRGs, appears to be the cause of the decreased PAH EQW, as opposed to extinction or grain destruction. Approximately 55% of LINER-like ULIRGs, 40% of HII-like ULIRGs, and 35% of cold ULIRGs have very low 6.2 μm PAH EQWs, indicative of buried AGN or starbursts with supressed PAH emission. Most of these ULIRGs also have high apparent silicate optical depths at 9.7 μm.

2. The apparent silicate optical depth is not correlated with far-infrared spectral slope. The ULIRGs with the strongest silicate absorption features have small 6.2 μm PAH EQWs and flat spectral slopes in the far-infrared. Their strong silicate absorption implies large columns of cold dust, but their small PAH EQWs and far-infrared colors imply substantial amounts of hot dust emission. For these sources, a model in which a warm source is viewed through either a smooth optically thick or clumpy dust shell seems inconsistent with the data.

3. ULIRGs with the largest rest-frame 24 μm luminosities have the smallest 6.2 μm PAH EQWs. A fit to our sample suggests $\log_{10}(6.2\ \mu\text{m PAH EQW}[\mu\text{m}]) = (7.71 \pm 0.07) + (-0.723 \pm 0.006) \times \log_{10}(\nu L_\nu(24\mu\text{m})[L_\odot])$. The range in PAH EQWs among luminous, high-redshift sources observed with Spitzer is much larger than implied by this correlation due to the presence of luminous sources with very large 6.2 μm EQWs. Extremely luminous sources of all types are rare at low-redshift, but those that do exist seem to be AGN dominated.

We would like to thank R. Chary, M. Lacy, J. Surace, and A. Sajina for insightful discussions. Support for this work was provided by NASA through an award issued by JPL/Caltech.

REFERENCES

Aitken, D. K., & Roche, P. F. 1985, MNRAS, 213, 777
Allen, D. A., Norris, R. P., Meadows, V. S., & Roche, P. F. 1991, MNRAS, 248, 528
Armus, L. et al. 2006, ApJ, 640, 204
—. 2007, ApJ, 656, 148
—. 2004, ApJS, 154, 178
Armus, L., Heckman, T., & Miley, G. 1987, AJ, 94, 831
Armus, L., Heckman, T. M., & Miley, G. K. 1989, ApJ, 347, 727
Borys, C. et al. 2006, ApJ, 636, 134
Brandl, B. R. et al. 2006, ApJ, 653, 1129
Burston, A. J., Ward, M. J., & Davies, R. I. 2001, MNRAS, 326, 403
Cutri, R. M., Huchra, J. P., Low, F. J., Brown, R. L., & Vanden Bout, P. A. 1994, ApJ, 424, L65
Dannerbauer, H., Rigopoulou, D., Lutz, D., Genzel, R., Sturm, E., & Moorwood, A. F. M. 2005, A&A, 441, 999
Davies, R. I., Sternberg, A., Lehnert, M., & Tacconi-Garman, L. E. 2003, ApJ, 597, 907
de Grijp, M. H. K., Miley, G. K., Lub, J., & de Jong, T. 1985, Nature, 314, 240
Desai, V. et al. 2006, ApJ, 641, 133
Duc, P.-A., Mirabel, I. F., & Maza, J. 1997, A&AS, 124, 533
Farrah, D. et al. 2007, ArXiv e-prints, 706
Franceschini, A., Aussel, H., Cesarsky, C. J., Elbaz, D., & Fadda, D. 2001, A&A, 378, 1
Genzel, R. et al. 1998, ApJ, 498, 579
Goldader, J. D., Joseph, R. D., Doyon, R., & Sanders, D. B. 1995, ApJ, 444, 97
Hao, L., Weedman, D. W., Spoon, H. W. W., Marshall, J. A., Levenson, N. A., Elitzur, M., & Houck, J. R. 2007, ApJ, 655, L77
Higdon, S. J. U. et al. 2004, PASP, 116, 975
Houck, J. R. et al. 2004, ApJS, 154, 18
—. 2005, ApJ, 622, L105
Imanishi, M., Dudley, C. C., Maiolino, R., Maloney, P. R., Nakagawa, T., & Risaliti, G. 2007, ApJS, 171, 72
Kim, D.-C., Veilleux, S., & Sanders, D. B. 1998, ApJ, 508, 627
Kleinmann, S. G., Hamilton, D., Keel, W. C., Wynn-Williams, C. G., Eales, S. A., Becklin, E. E., & Kuntz, K. D. 1988, ApJ, 328, 161
Kormendy, J., & Sanders, D. B. 1992, ApJ, 390, L53
Laurent, O., Mirabel, I. F., Charmandaris, V., Gallais, P., Madden, S. C., Sauvage, M., Vigroux, L., & Cesarsky, C. 2000, A&A, 359, 887
Le Floc'h, E. et al. 2005, ApJ, 632, 169
Levenson, N. A., Sirocky, M. M., Hao, L., Spoon, H. W. W., Marshall, J. A., Elitzur, M., & Houck, J. R. 2007, ApJ, 654, L45
Lutz, D., Spoon, H. W. W., Rigopoulou, D., Moorwood, A. F. M., & Genzel, R. 1998, ApJ, 505, L103
Lutz, D., Valiante, E., Sturm, E., Genzel, R., Tacconi, L. J., Lehnert, M. D., Sternberg, A., & Baker, A. J. 2005, ApJ, 625, L83
Lutz, D., Veilleux, S., & Genzel, R. 1999, ApJ, 517, L13
Menéndez-Delmestre, K. et al. 2007, ApJ, 655, L65
Moshir, M. 1990, in IRAS Faint Source Catalogue, version 2.0 (1990), 0–+

Murphy, Jr., T. W., Soifer, B. T., Matthews, K., Armus, L., & Kiger, J. R. 2001, AJ, 121, 97
Murphy, Jr., T. W., Soifer, B. T., Matthews, K., Kiger, J. R., & Armus, L. 1999, ApJ, 525, L85
Osterbrock, D. E., & De Robertis, M. M. 1985, PASP, 97, 1129
Pérez-González, P. G. et al. 2005, ApJ, 630, 82
Rigopoulou, D., Spoon, H. W. W., Genzel, R., Lutz, D., Moorwood, A. F. M., & Tran, Q. D. 1999, AJ, 118, 2625
Roussel, H. et al. 2006, ApJ, 646, 841
Sajina, A., Yan, L., Armus, L., Choi, P., Fadda, D., Helou, G., & Spoon, H. 2007, ArXiv e-prints, 704
Sanders, D. B., Mazzarella, J. M., Kim, D.-C., Surace, J. A., & Soifer, B. T. 2003, AJ, 126, 1607
Sanders, D. B., & Mirabel, I. F. 1996, ARA&A, 34, 749
Sanders, D. B., Soifer, B. T., Elias, J. H., Madore, B. F., Matthews, K., Neugebauer, G., & Scoville, N. Z. 1988a, ApJ, 325, 74
Sanders, D. B., Soifer, B. T., Elias, J. H., Neugebauer, G., & Matthews, K. 1988b, ApJ, 328, L35
Schweitzer, M. et al. 2006, ApJ, 649, 79
Scott, S. E. et al. 2002, MNRAS, 331, 817
Soifer, B. T. et al. 2000, AJ, 119, 509
Soifer, B. T., Sanders, D. B., Madore, B. F., Neugebauer, G., Danielson, G. E., Elias, J. H., Lonsdale, C. J., & Rice, W. L. 1987, ApJ, 320, 238
Spoon, H. W. W., Keane, J. V., Tielens, A. G. G. M., Lutz, D., Moorwood, A. F. M., & Laurent, O. 2002, A&A, 385, 1022
Spoon, H. W. W., Marshall, J. A., Houck, J. R., Elitzur, M., Hao, L., Armus, L., Brandl, B. R., & Charmandaris, V. 2007, ApJ, 654, L49
Stanford, S. A., Stern, D., van Breugel, W., & De Breuck, C. 2000, ApJS, 131, 185
Strauss, M. A., Huchra, J. P., Davis, M., Yahil, A., Fisher, K. B., & Tonry, J. 1992, ApJS, 83, 29
Sturm, E., Lutz, D., Verma, A., Netzer, H., Sternberg, A., Moorwood, A. F. M., Oliva, E., & Genzel, R. 2002, A&A, 393, 821
Sturm, E. et al. 2006, ApJ, 653, L13
Tran, Q. D. et al. 2001, ApJ, 552, 527
Valiante, E., Lutz, D., Sturm, E., Genzel, R., Tacconi, L. J., Lehnert, M. D., & Baker, A. J. 2007, ApJ, 660, 1060
Veilleux, S., Kim, D.-C., & Sanders, D. B. 1999a, ApJ, 522, 113
Veilleux, S., Kim, D.-C., Sanders, D. B., Mazzarella, J. M., & Soifer, B. T. 1995, ApJS, 98, 171
Veilleux, S., Sanders, D. B., & Kim, D.-C. 1997, ApJ, 484, 92
—. 1999b, ApJ, 522, 139
Voit, G. M. 1992, MNRAS, 258, 841
Weedman, D. W. et al. 2006, ApJ, 651, 101
Yan, L. et al. 2005, ApJ, 628, 604

TABLE 1
6.2 AND 11.3 μM PAH EQWS VERSUS SPECTRAL CLASS

		uncorrected 6.2μm PAH EQW		corrected 6.2μm PAH EQW		11.3 μm PAH EQW	
spectral class	number	median (μm)	average (μm)	median (μm)	average (μm)	median (μm)	average (μm)
HII	15	0.32	0.30 ± 0.16	0.28	0.27 ± 0.18	0.39	0.41 ± 0.20
LINER	22	0.19	0.27 ± 0.20	0.11	0.17 ± 0.14	0.50	0.46 ± 0.18
S1	6	0.02	0.04 ± 0.05	0.02	0.04 ± 0.05	0.03	0.03 ± 0.03
S2	21	0.05	0.10 ± 0.11	0.05	0.08 ± 0.07	0.09	0.16 ± 0.15
S1+S2	27	0.05	0.09 ± 0.10	0.04	0.07 ± 0.07	0.07	0.13 ± 0.14
Cold	66	0.30	0.32 ± 0.18	0.24	0.27 ± 0.18	0.50	0.52 ± 0.24
Warm	41	0.04	0.08 ± 0.09	0.04	0.06 ± 0.08	0.07	0.13 ± 0.13

NOTE. — Statistics on the 6.2 and 11.3 μm PAH EQWs of the ULIRGs in our sample, broken down by spectral class (Column 1). Column 2 gives the number of ULIRGs in each class. Columns 3 and 4 show the median and average 6.2 μm PAH EQWs, respectively, uncorrected for ice absorption. Columns 5 and 6 give the same statistics for the ice-corrected 6.2 μm PAH EQW (see Spoon et al. (2007) for details on this correction). Column 7 shows the median and average 11.3 μm PAH EQWs, uncorrected for the underlying silicate absorption. All medians and averages were computed by including sources with upper limits as though they were detections. Optical classifications are from Duc et al. (1997); Veilleux et al. (1997, 1995); Cutri et al. (1994); Allen et al. (1991); Armus et al. (1989); Kleinmann et al. (1988); Sanders et al. (1988b). The far-infrared classifications of cold ($f_\nu(25\mu m)/f_\nu(60\mu m) < 0.2$) and warm ($f_\nu(25\mu m)/f_\nu(60\mu m) \geq 0.2$) are based on the rest-frame 25 and 60 μm values calculated as described in §2.

TABLE 2
6.2 AND 11.3 μM PAH EQW VERSUS 24 μM LUMINOSITY

24 μm		uncorrected 6.2 μm PAH EQW		corrected 6.2 μm PAH EQW		11.3 μm PAH EQW	
Class	Luminosity ($10^{12}L_\odot$)	median (μm)	average (μm)	median (μm)	average (μm)	median (μm)	average (μm)
1	0.03 – 0.20	0.43	0.47 ± 0.16	0.41	0.41 ± 0.18	0.58	0.61 ± 0.20
2	0.20 – 0.30	0.33	0.34 ± 0.18	0.29	0.30 ± 0.17	0.56	0.52 ± 0.24
3	0.30 – 0.44	0.16	0.23 ± 0.17	0.10	0.17 ± 0.13	0.44	0.39 ± 0.18
4	0.44 – 0.63	0.14	0.17 ± 0.11	0.12	0.15 ± 0.11	0.31	0.30 ± 0.15
5	0.63 – 1.15	0.10	0.12 ± 0.10	0.06	0.07 ± 0.05	0.19	0.31 ± 0.40
6	1.15 – 8.00	0.03	0.04 ± 0.05	0.02	0.04 ± 0.05	0.05	0.08 ± 0.08

NOTE. — Same as Table 1, except the ULIRG sample is broken down into luminosity bins, rather than spectral class. Each bin contains 17-18 ULIRGs.

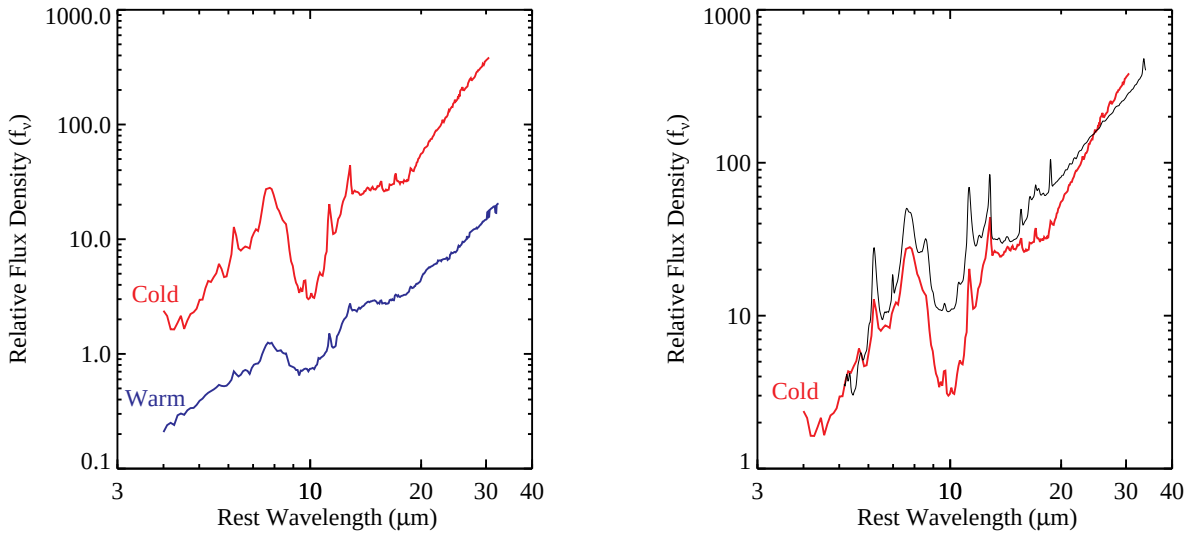

FIG. 1.— *Left:* The median IRS spectra of ULIRGs classified as cold (red) and warm (blue), arbitrarily normalized for display purposes. *Right:* The median spectrum of cold ULIRGs (red) compared to the average starburst spectrum from Brandl et al. (2006) (black), both normalized at 24 μm.

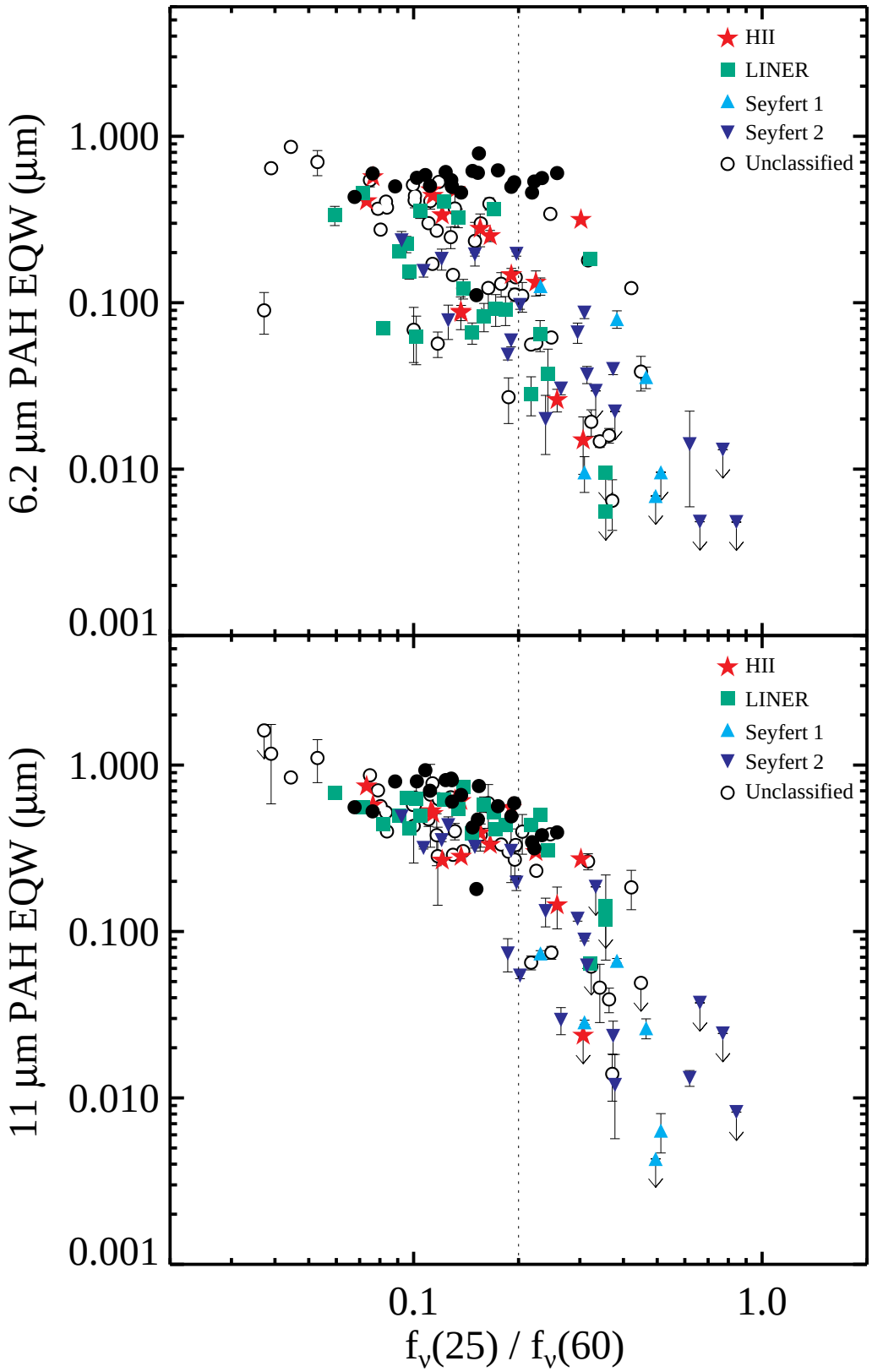

FIG. 2.— The 6.2 μm (top) and 11.3 μm (bottom) PAH EQW versus spectral slope. The ULIRGs are color-coded by optical spectroscopic classification: ULIRGs with HII-like optical spectra are plotted as red stars, LINER-like ULIRGs are shown as green squares, ULIRGs with Seyfert 1 optical spectra are shown as light blue triangles, ULIRGs with Seyfert 2 optical spectra are shown as dark blue upside-down triangles, and sources with unknown optical spectroscopic classifications are shown as white circles. The black dots represent the starburst galaxies from Brandl et al. (2006). The dotted vertical line represents the division between warm and cold sources adopted for this paper ($f_\nu(25)/f_\nu(60) = 0.2$), where cold sources lie to the left of the line and warm sources lie to the right.

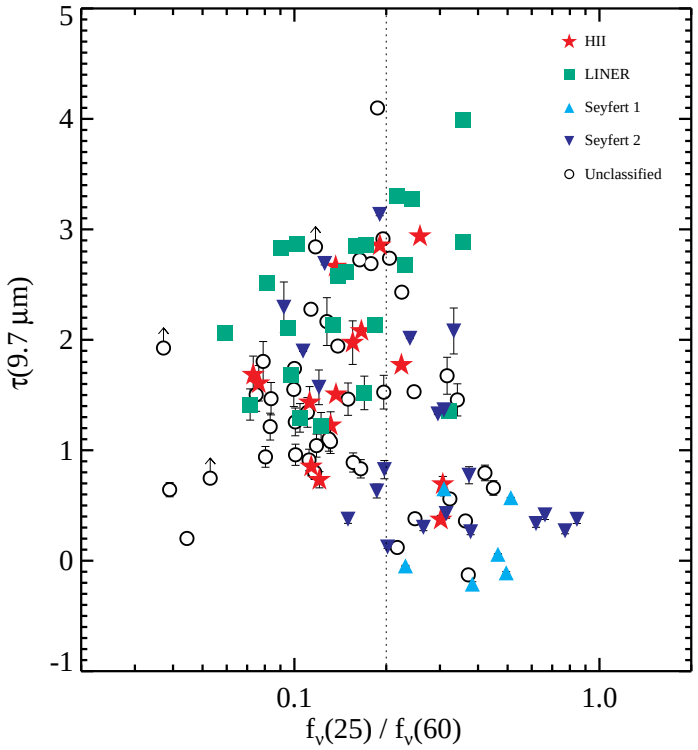

FIG. 3.— The 9.7 μm silicate optical depth versus the mid-infrared spectral slope. The ULIRGs are color-coded by optical spectroscopic classification, as in Figure 2. The vertical dotted line is $f_\nu(25)/f_\nu(60) = 0.2$, the division between warm and cold sources adopted for this paper. The spectral slope for the ULIRGs was computed from the IRS spectra as described in §2 and the spectral slope for the starbursts was computed from IRAS fluxes taken from Brandl et al. (2006).

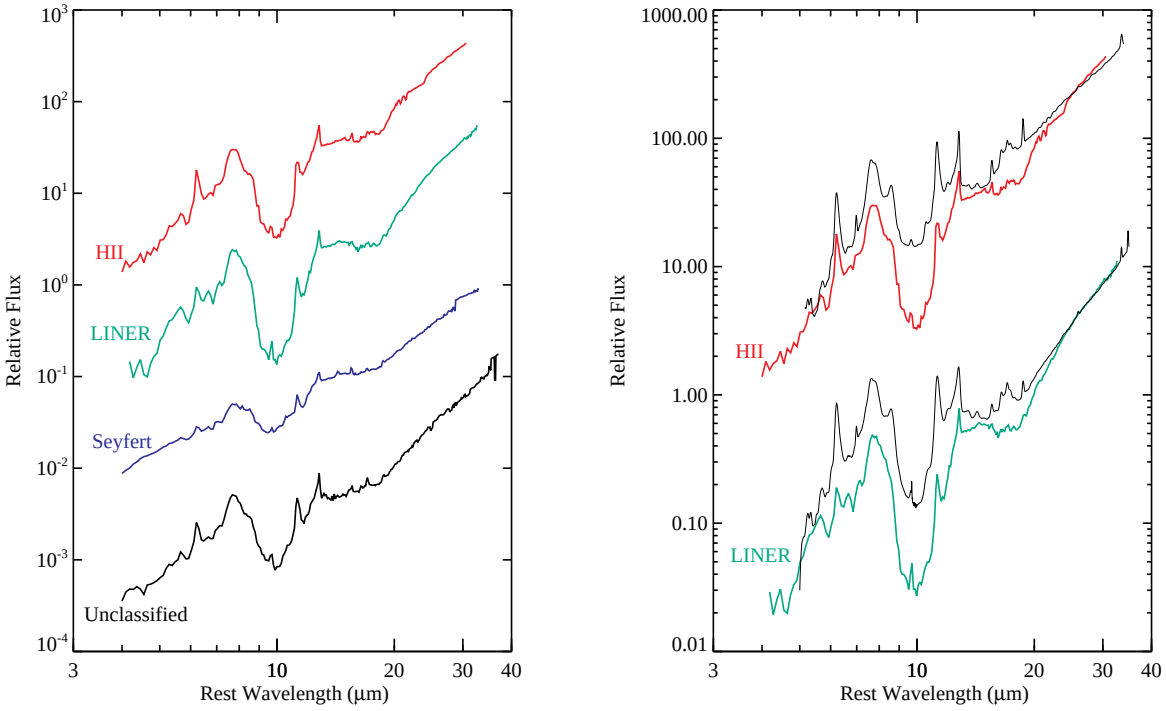

FIG. 4.— *Left:* The colored lines show the median IRS spectra of ULIRGs optically classified as HII-like (red), LINER-like (green), and Seyfert-like (blue). The black line shows the median spectrum of ULIRGs lacking optical classifications. The normalizations are arbitrary. *Right:* The median spectrum of HII-like ULIRGs compared to the average starburst spectrum from Brandl et al. (2006) (top red and black lines respectively) and the median spectrum of LINER-like ULIRGs compared to the average infrared-bright LINER spectrum from Sturm et al. (2006) (bottom green and black lines respectively). For wavelengths longer than 10 μm, the high-resolution Sturm et al. (2006) spectrum was convolved with a Gaussian profile with a FWHM of 0.2 μm to approximately match the resolution of the low-resolution ULIRG spectrum. The comparison spectra were normalized to match the HII- and LINER-like ULIRGs at 24 μm.

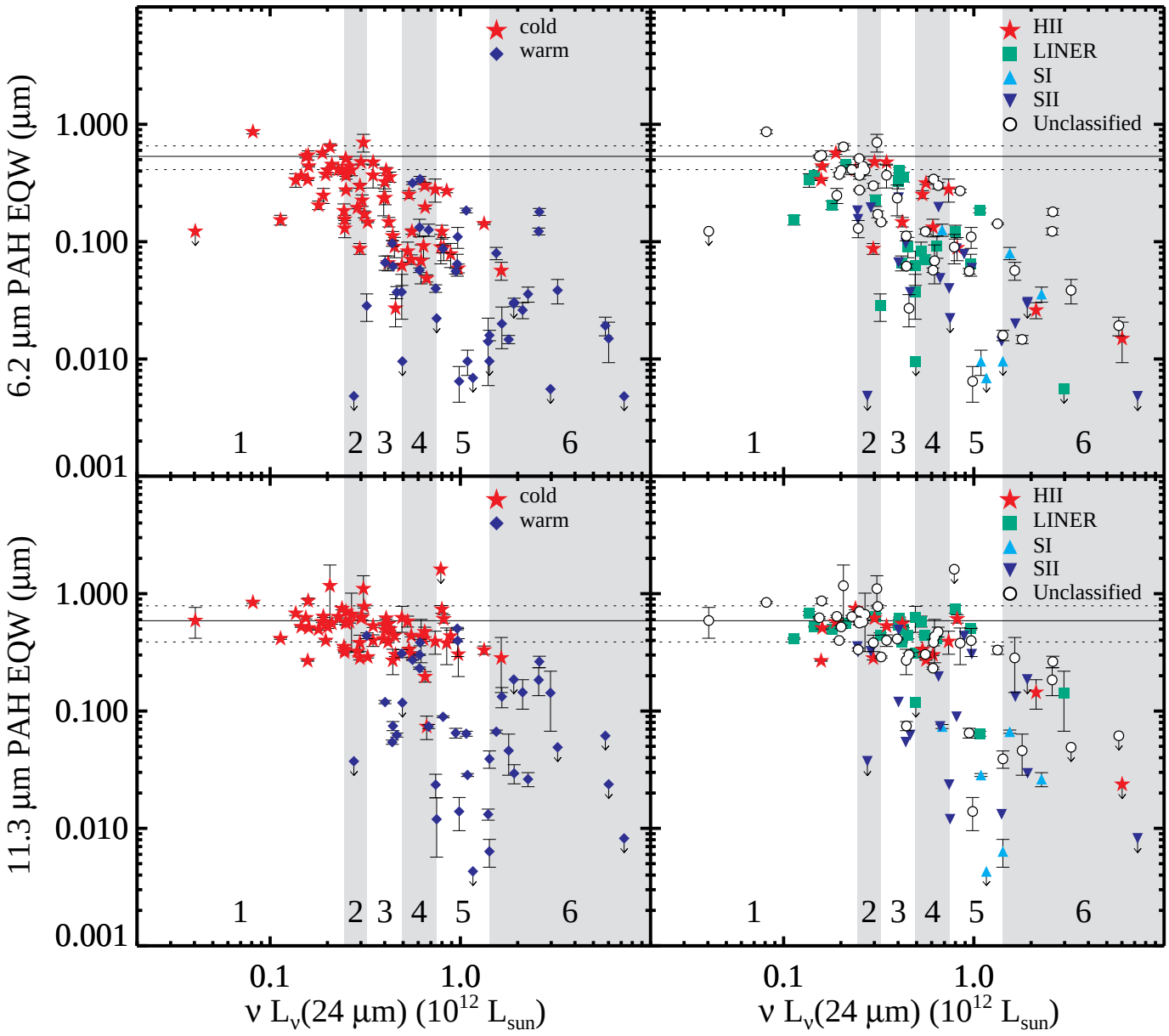

FIG. 5.— The 6.2 μm (top row) and 11.3 μm (bottom row) PAH EQWs versus 24 μm rest-frame luminosity. The ULIRG sample is color-coded by warm ($f_\nu(25\mu\mathrm{m})/f_\nu(60\mu\mathrm{m}) \geq 0.2$) and cold ($f_\nu(25\mu\mathrm{m})/f_\nu(60\mu\mathrm{m}) < 0.2$) mid-infrared spectral slope (left) and by optical spectroscopic classification as in Figure 3 (right). The average PAH EQWs of starburst galaxies from Brandl et al. (2006) are indicated by solid horizontal lines and the ± 1 σ dispersions in these averages are shown by dotted horizontal lines. Upper limits (3σ) to the PAH EQWs are indicated by downward pointing arrows. The six luminosity classes (1-6; see text and Table 2) are labeled on the bottom of each panel and are alternately shaded for clarity.

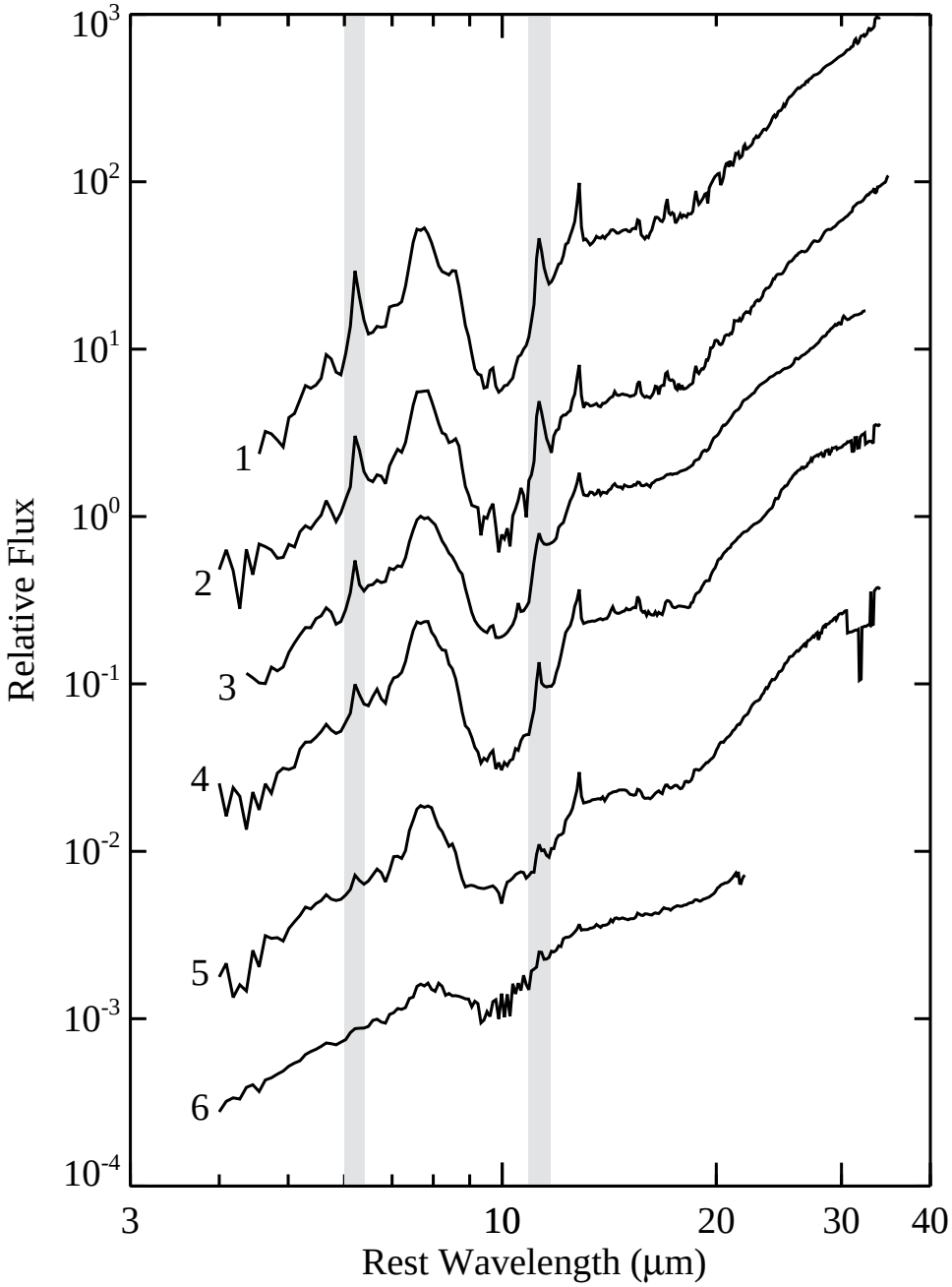

FIG. 6.— Median IRS ULIRG spectra for the six 24 μm rest-frame luminosity bins shown in Figure 5, arranged such that the luminosity increases from top to bottom. The grey bands highlight the positions of the 6.2 and 11.3 μm PAH features.

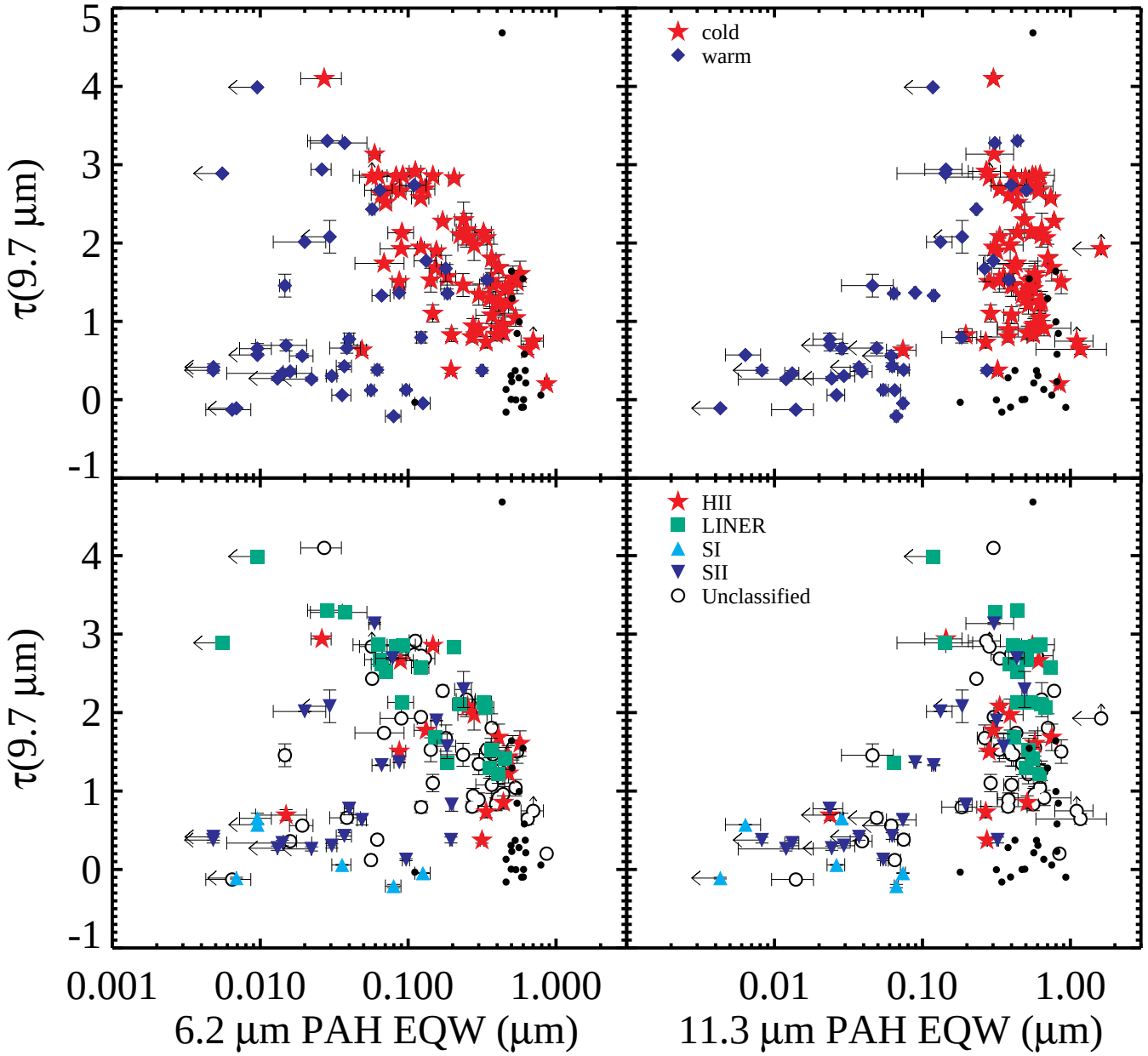

FIG. 7.— The strength of the 9.7 μm silicate absorption feature versus the 6.2 (left) and 11.3 (right) μm PAH EQWs. The ULIRGs are color-coded according to spectral slope and optical classification in the left and right panels, respectively. The colored symbols are identical to those in Figure 5. The small black dots represent the starbursts from Brandl et al. (2006).

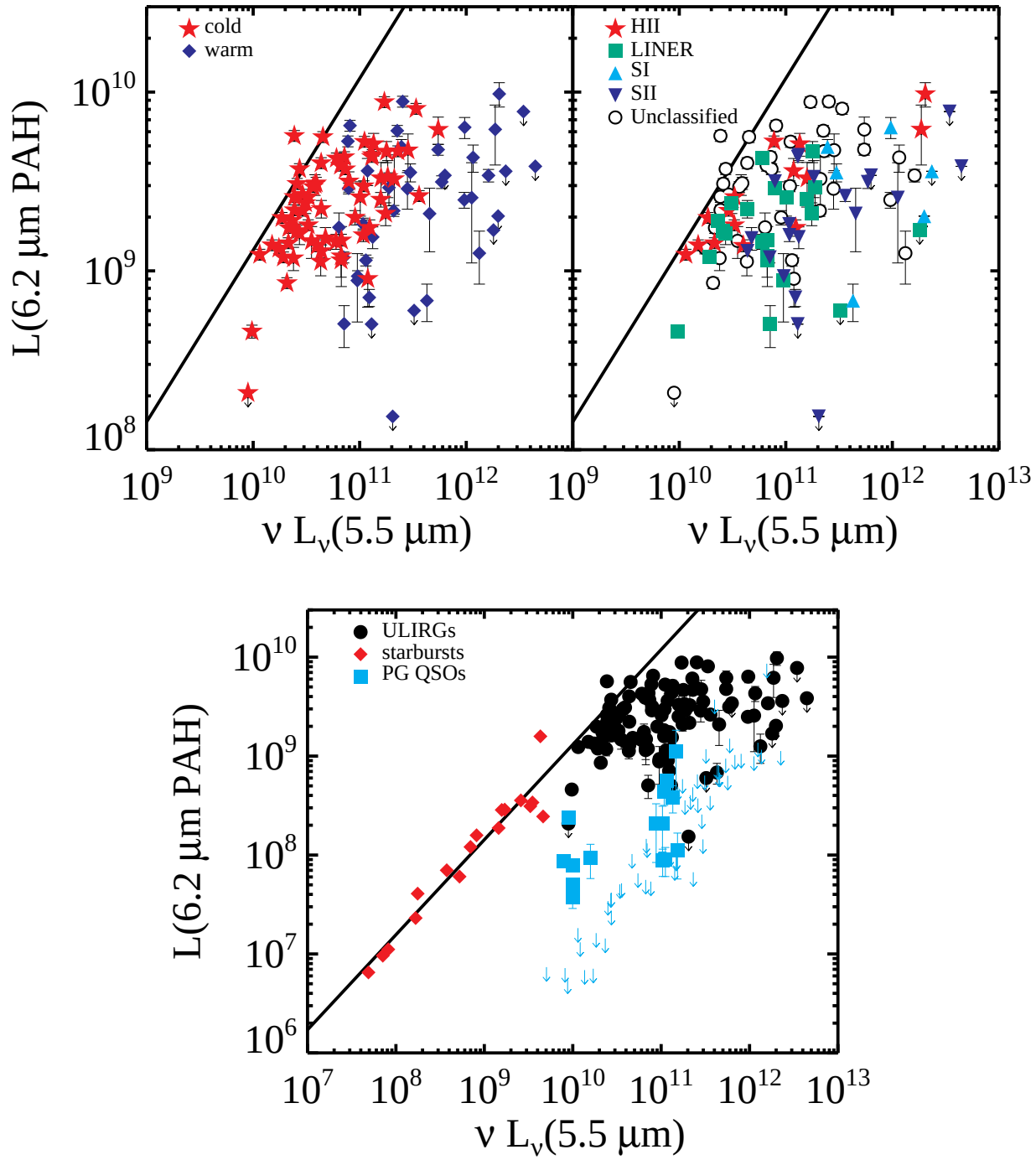

FIG. 8.— Luminosity in the 6.2 μm PAH feature as a function of 5.5 μm luminosity. In the top panels, the ULIRGs are color-coded according to spectral slope (left) and optical classification (right) using the same symbols as in Figure 5. The solid black line is a fit to the starbursts analyzed by Brandl et al. (2006). The bottom panel features expanded x and y axes to show the locations of the Brandl et al. (2006) starbursts (red diamonds) and ∼80 $z < 0.5$ PG QSOs, displayed as cyan squares (detections) and arrows (upper limits). In this bottom panel, the ULIRGs are shown as black circles.

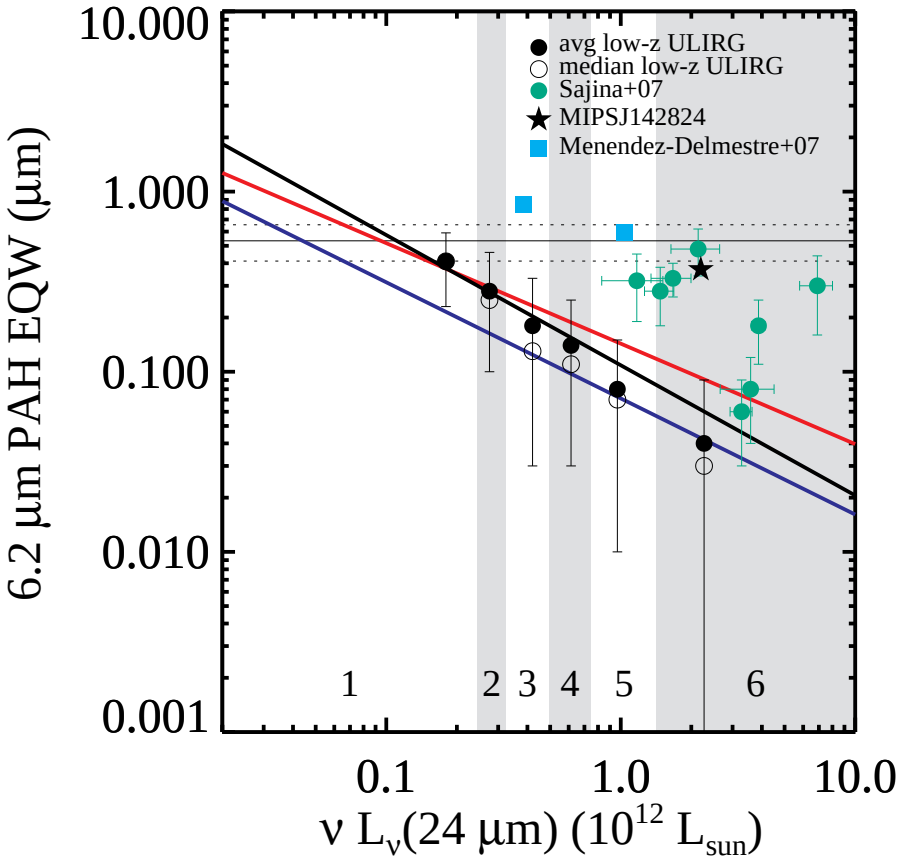

FIG. 9.— Median (open circles) and average (filled circles) 6.2 μm PAH EQW versus 24 μm luminosity. Both the medians and the means were computed by including sources with PAH EQW upper limits in the same way as detections. The error bars were computed as the dispersion in the PAH EQWs in each luminosity bin, and are centered on the average values in this plot. The x-position of each point is the median of the 24 μm luminosities of the sources in each luminosity bin. The thick red, blue, and black lines are fits to the cold ULIRGs, the warm ULIRGs, and all of the ULIRGs, respectively. Sources with upper limits on the PAH EQW were included in the fits as detections with 10% error bars. The horizontal thin and dotted black lines have the same meaning as in Figure 5, as do the luminosity bin labels across the bottom. The green points are the high-redshift ($z \sim 2$) ULIRGs from Sajina et al. (2007) with measured 6.2 μm PAH EQWs, and rest-frame 24 μm luminosities estimated from the 70 μm MIPS photometry. The large black star is MIPS J142824.0+352619, a bright 160 μm source at $z = 1.3$. The rest-frame 24 μm luminosity for this object was computed by via log-log interpolation of the photometry presented in Borys et al. (2006), and the 6.2 μm PAH EQW was taken from Desai et al. (2006).